Bioactive Materials 6 (2021) 2291–2302

Contents lists available at ScienceDirect

Bioactive Materials

journal homepage: www.sciencedirect.com/journal/bioactive-materials

Erythrocyte membrane-camouflaged carrier-free nanoassembly of FRET photosensitizer pairs with high therapeutic efficiency and high security for programmed cancer synergistic phototherapy

Xuanbo Zhang [a], Jianchen Xiong [a], Kaiyuan Wang [a], Han Yu [a], Bingjun Sun [a], Hao Ye [a], Zhiqiang Zhao [a], Ning Wang [a], Yuequan Wang [a], Shenwu Zhang [a], Wutong Zhao [a], Haotian Zhang [b], Zhonggui He [a], Cong Luo [a,**], Jin Sun [a,*]

[a] Department of Pharmaceutics, Wuya College of Innovation, Shenyang Pharmaceutical University, Shenyang, Liaoning, 110016, PR China
[b] School of Life Science and Biopharmaceutics, Shenyang Pharmaceutical University, Shenyang, 110016, PR China

ARTICLE INFO

Keywords:
FRET pair
Carrier-free
Nanoassembly
Erythrocyte membrane-camouflaged
Programmed synergistic phototherapy

ABSTRACT

Phototherapy has been intensively investigated as a non-invasive cancer treatment option. However, its clinical translation is still impeded by unsatisfactory therapeutic efficacy and severe phototoxicity. To achieve high therapeutic efficiency and high security, a nanoassembly of Forster Resonance Energy Transfer (FRET) photosensitizer pairs is developed on basis of dual-mode photosensitizer co-loading and photocaging strategy. For proof-of-concept, an erythrocyte-camouflaged FRET pair co-assembly of chlorine e6 (Ce6, FRET donor) and 1,1′-dioctadecyl-3,3,3′,3′-tetramethylindotricarbocyanine iodide (DiR, FRET acceptor) is investigated for breast cancer treatment. Notably, Ce6 in the nanoassemby is quenched by DiR and could be unlocked for photodynamic therapy (PDT) only when DiR is photobleached by 808-nm laser. As a result, Ce6-caused phototoxicity could be well controlled. Under cascaded laser irradiation (808–660 nm), tumor-localizing temperature rise following laser irradiation on DiR not only induces tumor cell apoptosis but also facilitates the tumor penetration of NPs, relieves tumor hypoxia, and promotes the PDT efficacy of Ce6. Such FRET pair-based nanoassembly provides a new strategy for developing multimodal phototherapy nanomedicines with high efficiency and good security.

1. Introduction

Breast cancer seriously threatens women's health [1,2]. Although most early-stage breast cancer can be effectively cured, triple negative breast cancer (TNBC) is still a great challenge in clinic [3,4]. TNBC is a subtype of breast cancer with negative estrogen receptor (ER), progesterone receptor (PR), and human epidermal growth factor receptor 2 (HER-2) [1]. The clinical features of TNBC mainly include poor sensitivity to chemotherapeutics drugs, high risk of remote metastasis, and poor prognosis of patients [5–9]. Therefore, the clinical treatment of TNBC with chemotherapy is still far from satisfactory [5,10]. Moreover, most chemotherapeutics agents have narrow therapeutic windows, resulting in serious side effects [11–13]. In addition to systemic chemotherapy, tumor-localized photodynamic therapy (PDT) and photothermal therapy (PTT) have also been extensively investigated as non-invasive cancer therapeutics for TNBC treatment [14].

PTT and PDT induce the apoptosis and/or necrosis of tumor cells via local temperature rise and reactive oxygen species (ROS) generation under laser irradiation, respectively [15,16]. Given that the therapeutic mechanisms of PTT and PDT are independent of the expression of specific cell receptors, phototherapy has been considered as ideal treatment regimen for TNBC [17,18]. However, the therapeutic efficacy of mono-phototherapy (PTT or PDT alone) is far from satisfactory [19–21]. PTT, with spatial heterogeneous distribution of temperature rise within tumor tissues, is not sufficient to completely eliminate the tumor cells [22–24]. Moreover, the production of ROS by most photosensitizers (PSs) for PDT heavily depends on oxygen. As a result, the tumor hypoxia has posed a big obstacle for PDT [16,25]. Notably, the combination of

Peer review under responsibility of KeAi Communications Co., Ltd.
* Corresponding author.
** Corresponding author.
E-mail addresses: luocong@syphu.edu.cn (C. Luo), sunjin@syphu.edu.cn (J. Sun).

https://doi.org/10.1016/j.bioactmat.2021.01.004
Received 28 October 2020; Received in revised form 22 December 2020; Accepted 5 January 2021

PDT and PTT can achieve complementary advantages [26]. On the one hand, tumor-localized temperature rise via PTT can not only induce tumor cell apoptosis but also improve the blood perfusion at the tumor site, which could significantly relieve tumor hypoxia, thus facilitating the therapeutic efficacy of PDT [16,27]. On the other hand, the generated ROS could in turn promoting the PTT-mediated anticancer therapy [22,28].

Despite the promising application of PTT/PDT combo, serious phototoxicity still brings great agony and inconvenience to cancer patients, especially the ROS-induced normal tissue damage after PDT [16,29,30]. Although most PSs show no cytotoxicity without laser irradiation, patients have to avoid being exposed to light for a long time to wait for the complete metabolism and excretion of PSs from the body [15,31]. Additionally, potential damage to the neighboring normal tissues around tumors caused by the inevitable laser exposure during the therapeutic process usually leads to serious toxic side effects [29]. Therefore, how to achieve high-efficiency combination drug delivery with controllable phototoxicity is of crucial importance for PTT/PDT multimodal cancer therapy [16,30].

Pure drug-driven nanoassembly has attracted great interests in developing high-efficient drug delivery systems [12–14,32,33]. Particularly, the development of drug pair-based co-assembled nanosystems has emerged as a promising strategy for combination therapy [33,34]. Herein, we reported a co-assembly strategy of FRET pairs with dual-mode photosensitizer co-loading and phototoxicity locking for programmed cascade-activatable PTT/PDT. Several photothermal and photodynamic FRET pairs were found to readily co-assemble into uniform nanoparticles (NPs) with locked phototoxicity. For proof-of-concept, we focused on the construction of an erythrocyte-camouflaged nanoassembly of Ce6 and DiR (Ce6@DiR-M NPs) for TNBC treatment (Fig. 1). The FRET pair of Ce6 and DiR co-assembled into uniform NPs (Ce6@DiR NPs), and the erythrocyte camouflaged coating technique was utilized not only to stabilize Ce6@DiR NPs but also to improve pharmaceutic pharmacokinetic behavior in multiple dosing [35]. Notably, Ce6 was quenched by DiR in the nanoassembly due to the FRET interaction, which "turned off" the photosensitivity of Ce6. Only after DiR was photobleached with 808 nm laser, the PDT function of Ce6 could be "turned on", by which the undesired ROS-induced phototoxicity of Ce6 could be efficiently reduced. Such a FRET pair-based nanoassembly was supposed to perform as a versatile co-delivery nanosystem with synergetic phototherapy and high security.

2. Results and discussions

2.1. Co-assembly of FRET photosensitizer pairs with photocaged ROS generation

To demonstrate the generality of FRET photosensitizer pair co-assembly strategy, we screened four different kinds of organic photodynamic photosensitizers including two porphyrin derivatives (Ce6 and pheophorbide-a, PPa), a phthalocyanine (zinc phthalocyanine, ZnPc), a BODIPY dye (3-Bodipy-propanoic acid, BDP) and a natural product derived from hypericum (hypericin, Hy) with DiR, a cyanine dye used as

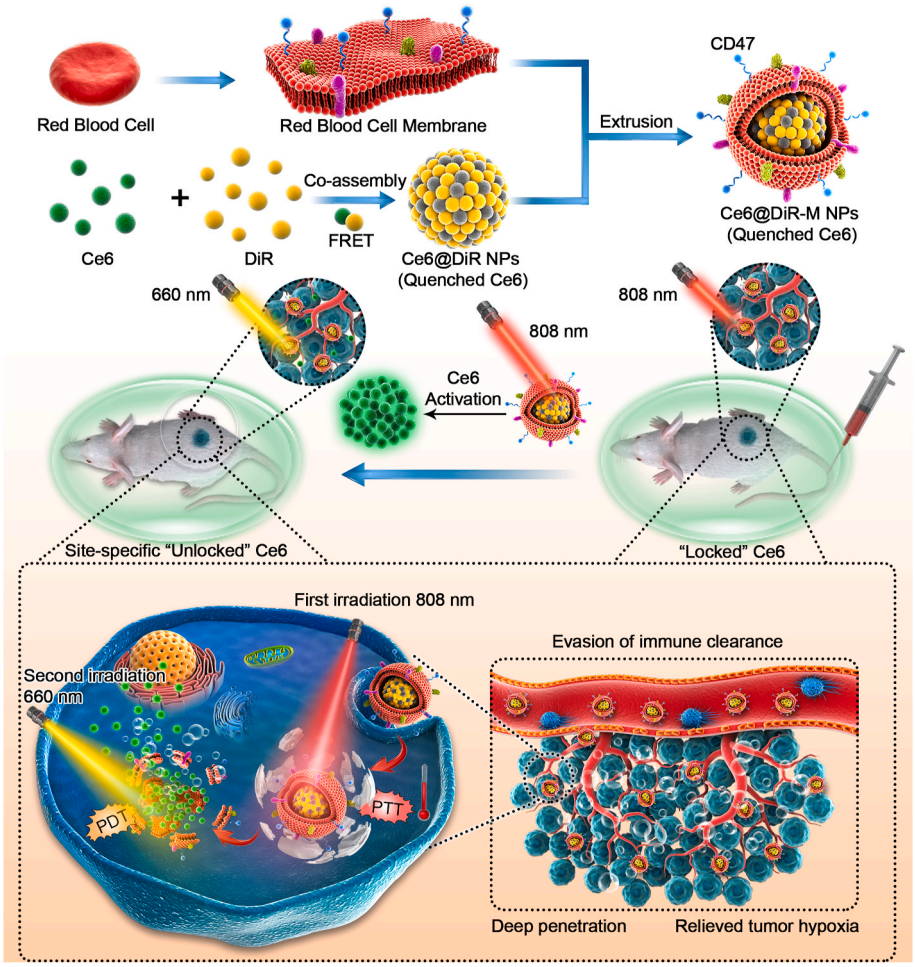

Fig. 1. Schematic representation of the preparation of erythrocyte camouflaged Ce6@DiR NPs (Ce6@DiR-M NPs) and its programmed cascade-activatable photothermal-photodynamic therapy for TNBC with low phototoxicity in normal tissues.

photothermal photosensitizers (PTP) (Fig. 2A). Interestingly, all these photodynamic photosensitizers formed uniform nanoassemblies with DiR, implying the promising potential of carrier-free FRET pair co-assembly strategy for highly efficient co-delivery of hydrophobic organic photosensitizers (Fig. 2B–D). The spectral overlap between DiR and photodynamic photosensitizers (PDP) suggested that DiR could be an effective FRET acceptor of these PDP (Fig. 2E). The FRET interaction might reduce the ROS production of PDP [16], therefore, the singlet oxygen-generation capacity of the PDP and co-assembled NPs were directly explored with Singlet Oxygen Sensor Green (SOSG). As shown in Fig. 2F, compared with photosensitizer solutions (Sol), ROS generation from the co-assemblies was significantly reduced, implying ROS-generation locking ability of the FRET pair co-assembly strategy, which would benefit to alleviating ROS-induced phototoxicity towards normal tissues.

2.2. Erythrocyte camouflaged Ce6@DiR co-assembly

We then focused on the nanoassembly of Ce6 and DiR (Ce6@DiR NPs) to further investigate programmed cancer synergistic phototherapy, and biomimetic technology of cell membrane camouflage was used to improve the *in vivo* behavior of NPs in multiple dosing. The co-assembled Ce6@DiR NPs were prepared using a facile one-step nanoprecipitation method. Similarly, Ce6 alone precipitated immediately in deionized water (Fig. S1), while DiR and Ce6 could co-assemble into uniform NPs (Fig. 3A), and the optimized molar ratio of Ce6 to DiR was determined as 1: 1.5 (Fig. S1 and Table S1) with the average diameter around 97.5 nm and Zeta potential around −10 mV. Subsequently, the Ce6@DiR-M NPs were fabricated by extruding the mixture of Ce6@DiR NPs and red blood cell membranes (RBCMs) at an optimal weight ratio of 1:5 (Fig. S2 and Table S2). Compared with Ce6@DiR NPs, the average diameter of Ce6@DiR-M NPs increased by about 30 nm, and the Zeta

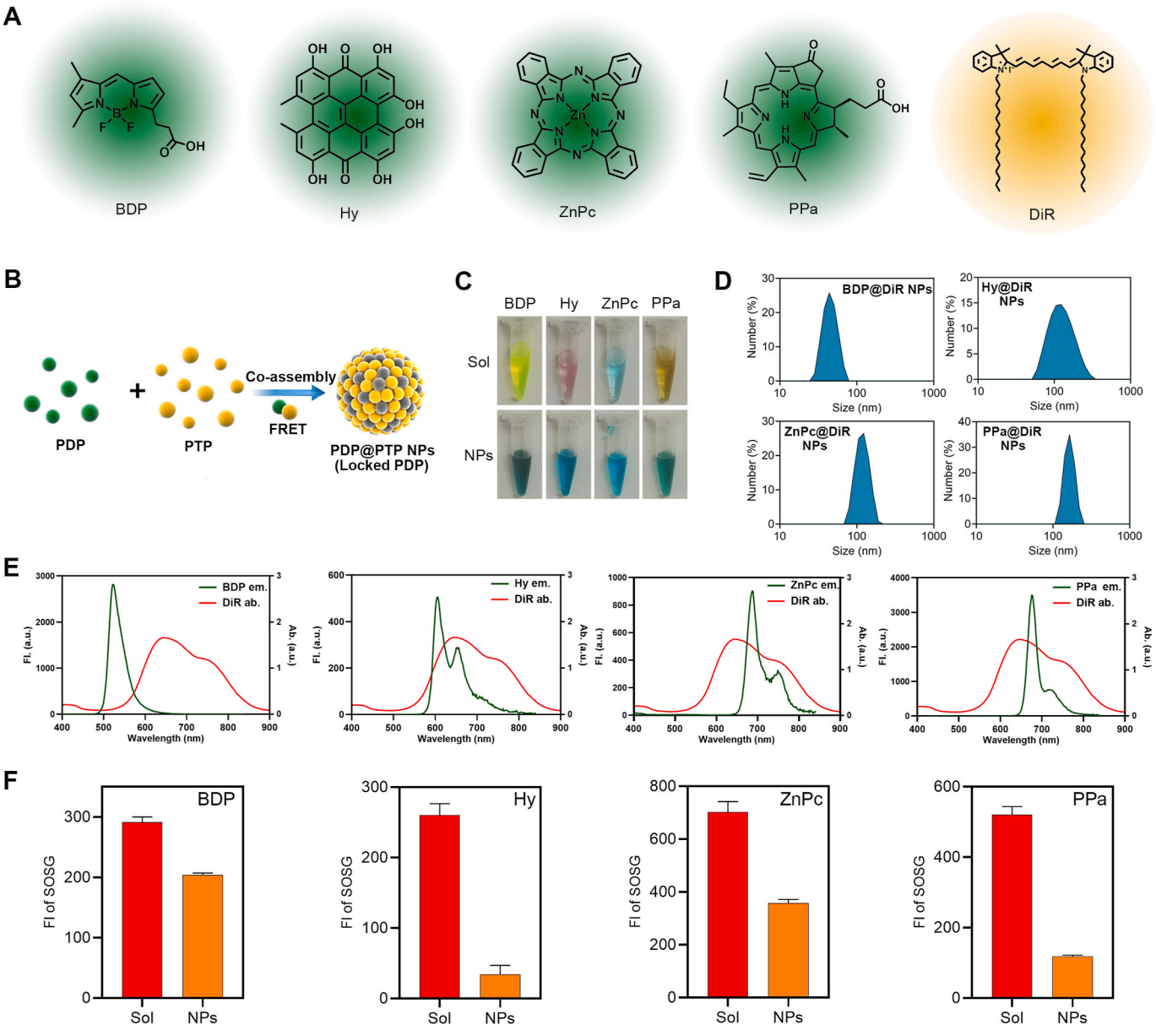

Fig. 2. Co-assembly of PTP @ PDP and reducing PDP-generated ROS. (A) Molecular structures of PDP (green) and PTP (yellow). (B) Schematic illustration of the FRET pair co-assembled process. (C) Photo of PDP Sol and NPs co-assembled with DiR. (D) Particle size results of NPs in number %. (E) Spectra of PDP FRET-donor (BDP, Hy, ZnPc, and PPa) emission with PTP FRET-acceptor (DiR) absorption. (F) Singlet oxygen generation (detected by SOSG) of the PDP (irradiated by 660 nm laser, 10 mW cm^{-2}, 15min).

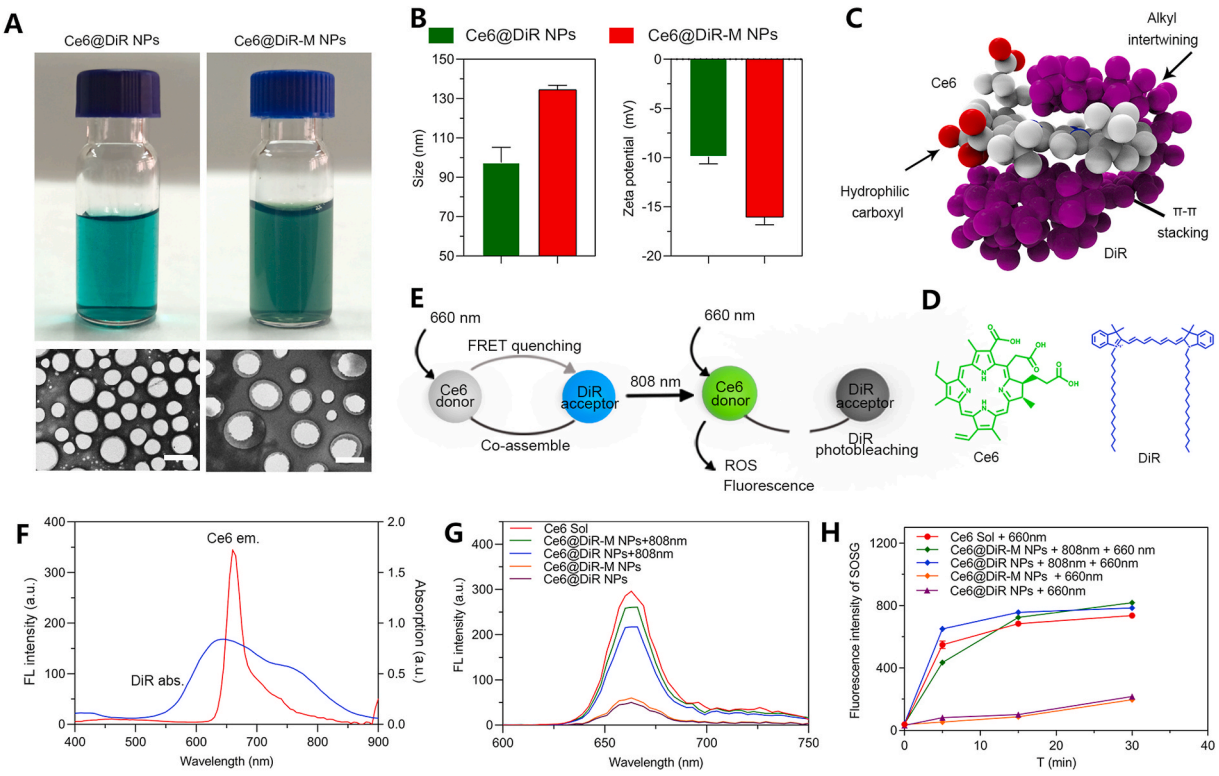

Fig. 3. Co-assemble of Ce6 with DiR and the quenching and activation of Ce6 molecules. (A) Photographs and TEM images, the scale bar represents 100 nm; (B) Hydrodynamic diameter and zeta potential; (C) Molecular docking of Ce6 (white) and DiR (purple); (D) Molecular structures; (E) Schematic illustration of the activation of quenched Ce6 with cascaded laser irradiation (808 nm–660 nm). (F) Spectra of DiR acceptor absorption and Ce6 donor emission; (G) Fluorescence spectrum and (H) Singlet oxygen generation abilities (irradiated by 660 nm laser, 10 mW cm^{-2} for 5min) of the co-assemblies before and after 808 nm laser irradiation (1 W cm^{-2}, 5 min).

potential also slightly increased to −16.1 ± 0.8 mV (Fig. 3A and B). Transmission electron microscopy (TEM) images also revealed the successful fabrication of erythrocyte camouflaged Ce6@DiR-M NPs (Fig. 3A). Both the sodium dodecyl sulfate polyacrylamide gel electrophoresis (SDS-PAGE) and western blotting results showed the presence of typical CD47 molecules on the surface of Ce6@DiR-M NPs (Figs. S3A and S3B). Additionally, both the Ce6@DiR-M NPs and Ce6@DiR NPs showed good colloidal stability in PBS containing 10% FBS for 12 h (Fig. S4).

2.3. Co-assembly mechanisms of Ce6 and DiR

The molecular docking technique was utilized to explore the co-assembly mechanism of DiR and Ce6. As shown in Fig. 3D, multiple interactions could be found in the co-assembled NPs of DiR and Ce6, including: (i) π-π stacking between the porphyrin ring of Ce6 and the aromatic head of DiR; (ii) the alkyl intertwining between them; and (iii) the opposite charge interactions between them. As shown in Fig. 3C, the molecular docking result revealed a "scorpion-like" structure of Ce6 and DiR, with a binding energy of −4.7 kcal/mol. The aromatic head of the DiR and porphyrin ring of Ce6 could form a strong π-π-stacking force, and the two long alkyl chains of DiR "wrapped" the plane structure of Ce6 to make the intermolecular binding much tighter. Moreover, the charge interactions between the carboxyl groups of Ce6 and the tertiary amines of DiR could also significantly increase their intermolecular affinity. As a result, multiple intermolecular interactions between DiR and Ce6 endow them with the co-assembly capacity to form stable nanostructures (Figs. 3A and S4).

2.4. In vitro photothermal effect and activation of quenched Ce6

We then investigated the photothermal efficiency of Ce6@DiR-M NPs *in vitro*. With an 808 nm laser irradiation for 3 min at 2 W cm^{-2}, the temperature could be readily heated more than 40–50 °C under laser treatment for 3 min (Fig. S5), and the viability of tumor cells could be decreased under such a condition. The photobleaching of DiR with 808-nm laser irradiation was also expected to unlock the photosensitivity of Ce6 molecules in the nanoassembly (Fig. 3E). As shown in Fig. 3E–G, since the absorption of DiR acceptor had a significant overlap with Ce6 emission, the fluorescence of Ce6 was quenched by DiR in the nanoassembly, but the emitted fluorescence intensity of Ce6 was significantly increased upon the photobleaching of DiR. And the appearance and morphology of Ce6@DiR NPs and Ce6@DiR-M NPs significantly changed following the irradiation (Fig. S6). Furthermore, we investigated the influence of DiR photobleaching on the singlet oxygen generation of Ce6@DiR NPs and Ce6@DiR-M NPs. As shown in Fig. 3H, both Ce6@DiR NPs and Ce6@DiR-M NPs showed very low singlet oxygen-generation ability before receiving 808-nm irradiation. By contrast, Ce6@DiR NPs and Ce6@DiR-M NPs had a comparable yield of singlet-oxygen with Ce6 Sol after receiving cascaded laser irradiation (808 nm–660 nm). These results confirmed our hypothesis that the quenched Ce6 in the FRET-paired nanoassembly could be efficiently turned on upon the photobleached exhaustion of DiR.

2.5. Cellular uptake and in vitro photo cytotoxicity

The cellular uptake and intracellular Ce6 activation of Ce6@DiR NPs and Ce6@DiR-M NPs were investigated on 4T1 murine breast cancer cells. As shown in Figs. 4A and S7, cells incubated with Ce6@DiR NPs and Ce6@DiR-M NPs showed very weak fluorescent signals of Ce6 at

both 0.5 and 2 h. Notably, when the cells received 808-nm laser treatment (1 W cm^{-2}, 5 min), the fluorescence intensity of both Ce6@DiR NPs and Ce6@DiR-M NPs was recovered suggesting the quenched Ce6 in the nanoassemblies could be readily unlocked upon the photobleaching of DiR. Furthermore, intracellular oxidative stress was measured by DCFH-DA. Similarly, Ce6@DiR NPs/Ce6@DiR-M NPs demonstrated much higher intracellular oxidative stress under programmed laser treatment comparing with the locked NPs (without 808-nm laser treatment) (Fig. S8). We then evaluated the influence of DiR photobleaching on the ROS-induced cytotoxicity of Ce6@DiR NPs and Ce6@DiR-M NPs (Fig. 4B). Compared with Ce6 Sol, Ce6@DiR NPs and Ce6@DiR-M NPs showed negligible cytotoxicity with 660-nm laser irradiation (1.5 mW cm^{-2}, 5 min) (Fig. 4C and Table S3). By contrast, the cytotoxicity of Ce6@DiR NPs and Ce6@DiR-M NPs significantly increased after the photobleaching of DiR using a mild 808-nm laser (1 W cm^{-2}, 5 min), which had little influence on the cell viability (Fig. S9). Moreover, Ce6 Sol, Ce6@DiR NPs, and Ce6@DiR-M NPs presented negligible cytotoxicity without laser irradiation (Fig. S10). Additionally, the combined cytotoxicity of PTT and PDT was further conducted using a high-power 808-nm laser (3 W cm^{-2}, 3 min) and the same 660-nm laser (1.5 mW cm^{-2}, 5 min). As shown in Fig. 4D and Table S4, both Ce6@DiR NPs and Ce6@DiR-M NPs showed significantly increased cytotoxicity when compared with mono phototherapy, due to the higher cellular uptake efficiency and synergetic phototherapy. These results revealed that activation of Ce6 in Ce6@DiR NPs and Ce6@DiR-M NPs could be well controlled by DiR photobleaching, which could be utilized to guarantee the therapeutic safety of the FRET pair-based nanoassembly via avoiding ROS-induced off-target phototoxicity.

As previously discussed, tumor-localizing temperature rise by DiR might not only induces tumor cell apoptosis but also facilitates the deep tumor penetration of the co-assembled NPs. To test the hypothesis, the tumor spheroids were incubated with Ce6 Sol and Ce6@DiR-M NPs at an equivalent Ce6 dose of 0.67 μM for 4 h and received different laser treatments. As shown in Fig. 4E, the Ce6@DiR-M NPs-treated spheroid with laser irradiation (3.0 W cm^{-2}) showed much stronger fluorescence signals than that of the Ce6 Sol-treated group, especially deep inside the spheroid. The improved penetration capacity should be attributed to the increased space between cells in the spheroid caused by temperature rise and partial cell apoptosis. By contrast, the Ce6@DiR-M NPs-treated spheroid without laser irradiation (1.0 W cm^{-2}) exhibited even weaker

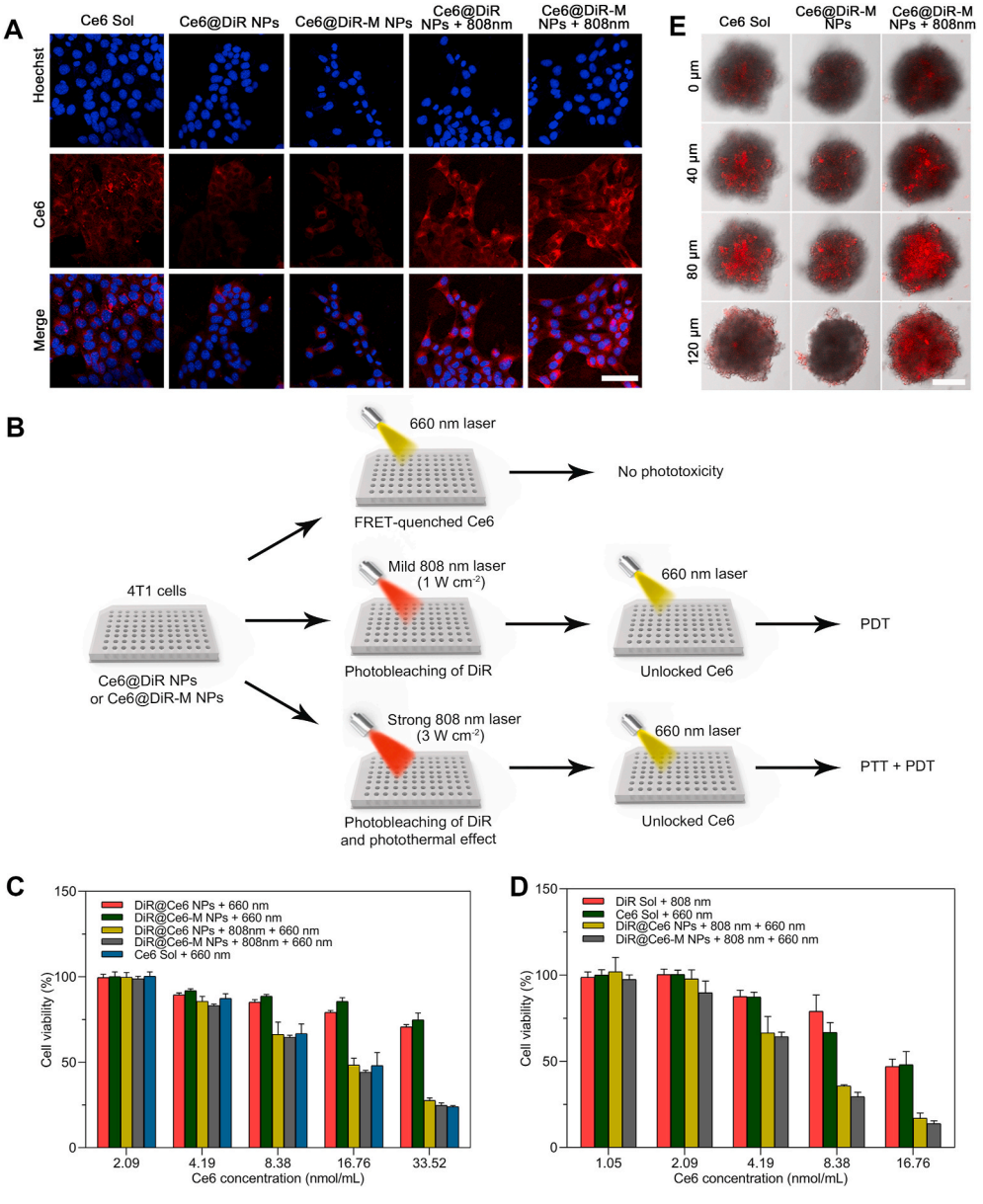

Fig. 4. Cellular uptake and *in vitro* photo cytotoxicity of activated and quenched Ce6 in the co-assemblies. (A) CLSM images of Ce6 Sol, Ce6@DiR NPs and Ce6@DiR-M NPs at 2 h (with or without irradiation under 808-nm laser before observation) (the scale bar represents 50 μm); (B) Schematic image of different irradiation treatments on 4T1 murine breast cancer cells incubated with Ce6@DiR-M NPs and its corresponding results. (C) Photo cytotoxicity of Ce6 in the co-assemblies before and after the photobleaching of DiR (1.5 mW cm^{-2} and 5 min of 660-nm laser, 1.0 W cm^{-2} and 5 min of 808-nm laser); (D) Combined cytotoxicity of PTT and PDT (1.5 mW cm^{-2} and 5 min of 660-nm laser, 3.0 W cm^{-2} and 3 min of 808-nm laser); (E) Tumor spheroids-penetration of the co-assemblies after 808-nm laser irradiation (3 W cm^{-2} and 3 min at 2 h) (the scale bar represents 150 μm).

fluorescence signals than that of Ce6 Sol-treated group, due to the inferior mobility and permeability of NPs compared with small-molecule drugs. These results confirmed our hypothesis that the tumor-localizing temperature rise by DiR not only kills tumor cells but also facilitates the tumor penetration of NPs. It could help relieve tumor hypoxia and facilitate the PDT efficacy of Ce6 in the *in vivo* tumor-bearing animal models.

2.6. Haemolysis and pharmacokinetics

The hemolytic experiment of NPs was studied. As shown in Fig. S11, there's no obvious hemolysis of RBC was observed, suggesting good biocompatibility of the nanosystem in blood. The pharmacokinetic profiles of the co-assembled NPs were further studied in Sprague-Dawley (SD) rats by determining the fluorescence intensity of DiR in plasma after being extracted using methanol, in which the nanoassembly was destroyed. As shown in Fig. 5A and Table S5, free DiR Sol was quickly cleared from the body after intravenous administration. In contrast, even the naked nanoassembly of DiR and Ce6 (Ce6@DiR NPs) could extend the circulation time in blood. Notably, the erythrocyte camouflaged nanoassembly (Ce6@DiR-M NPs) significantly prolonged retention of DiR in blood compared to DiR Sol and Ce6@DiR NPs, even better than the PEGylated formulation (Ce6@DiR-PEG NPs). More importantly, Ce6@DiR-M NPs could effectively address the dilemma of PEGylation modification. As shown in Fig. 5B and C, and Table S6, the second dose of Ce6@DiR-PEG NPs drastically accelerated its clearance, while the second dose of Ce6@DiR-M NPs didn't change much. The improved pharmacokinetic behavior of Ce6@DiR-M NPs could be attributed to the improved stability and immune escape of RBCM. The CD47 expressed on RBCM (Fig. S3) is a "don't eat me" marker allowing the escape of Ce6@DiR-M NPs from immune clearance [35].

2.7. Biodistributions

The FRET-paired nanoassembly of Ce6 and DiR could serve as a self-tracing nanosystem with a near-infrared dye (DiR) loaded in the NPs. Therefore, the biodistributions of DiR Sol, Ce6@DiR NPs, and Ce6@DiR-M NPs were explored by monitoring the DiR fluorescence in the 4T1 tumor-bearing mice xenograft model. At 24 h post-administration, all the mice were killed and the *ex vivo* biodistribution in main organs and tumors was taken out to further quantify the fluorescence intensity of DiR. As shown in Fig. 5D, E, and 5F, negligible fluorescence signals were found in the tumors of DiR Sol-treated mice. By contrast, both Ce6@DiR NPs and Ce6@DiR-M NPs showed significantly increased fluorescence signals of DiR over time from 1 h to 24 h, and Ce6@DiR-M NPs revealed higher tumor accumulation than that of Ce6@DiR NPs. The increased intratumoral accumulation of Ce6@DiR-M NPs should be attributed to the long systemic circulation time and the enhanced permeability and retention (EPR) effect.

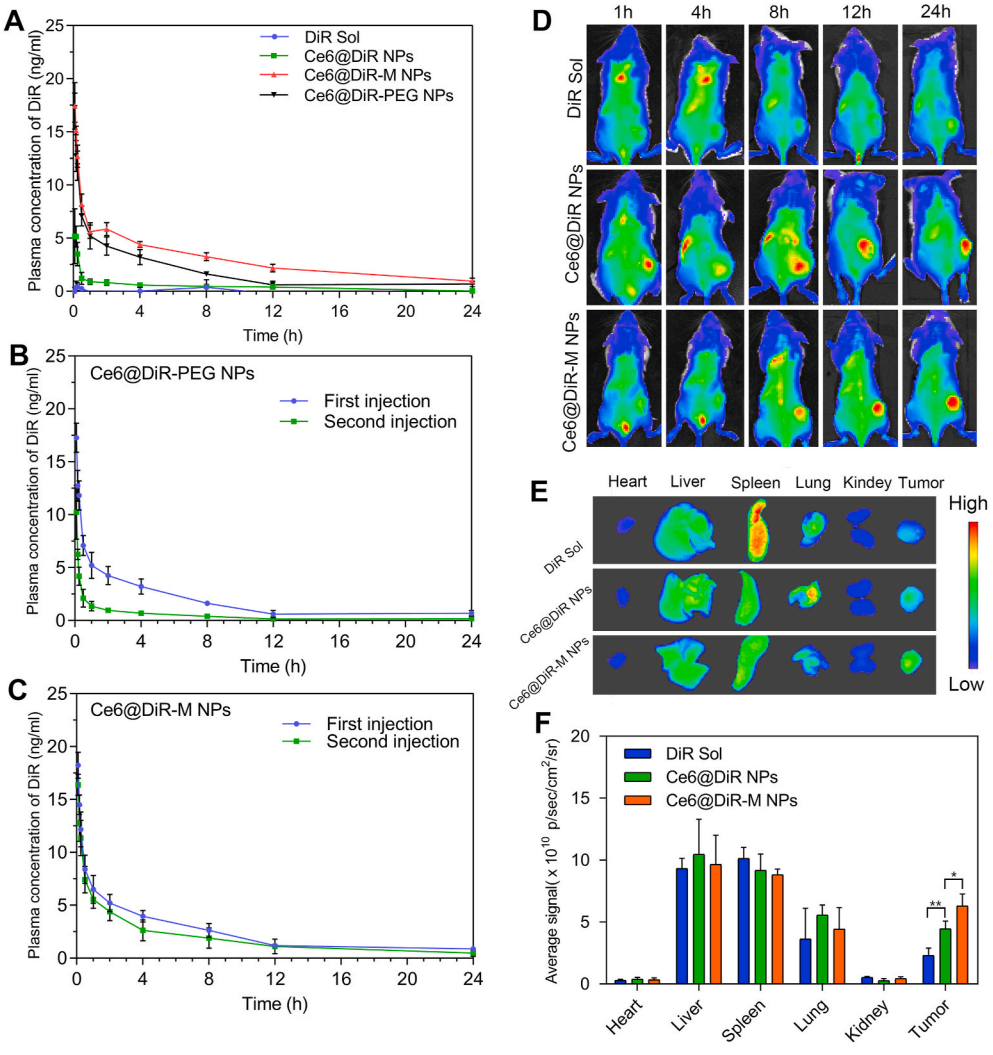

Fig. 5. *In vivo* pharmacokinetics and biodistribution studies. (A) Pharmacokinetic studies at the first dose of DiR Sol, Ce6@DiR NPs, Ce6@DiR-PEG NPs, and Ce6@DiR-M NPs; Pharmacokinetics studies of the first and second dose of (B) Ce6@DiR-PEG NPs and (C) Ce6@DiR-M NPs (All of these formulations were intravenous injected at an equivalent DiR dose of 1 mg kg^{-1} (n = 5)); (D) *In vivo* biodistributions of DiR Sol, Ce6@DiR NPs and Ce6@DiR-M NPs at different time intervals; (E) Ex vivo biodistributions and (F) quantitative results at 24 h post-injection. The data are presented as means ± SD, $^{*}P < 0.05$ and $^{**}P < 0.01$.

2.8. *In vivo* photothermal effect and modulation of the tumor hypoxia

Multiple drug delivery advantages make Ce6@DiR-M NPs as promising nanomedicine for *in vivo* evaluation of antitumor activity (Fig. 6A). The *in vivo* antitumor activity was explored in the 4T1 tumor-bearing mouse xenograft model. The photothermal efficiency *in vivo* was firstly evaluated. As shown in Fig. 6B and C, Ce6@DiR-M NPs exhibited distinct temperature rising at the tumor site compared with Ce6@DiR NPs and DiR Sol. It has been found that tumor-localized temperature rising helps relieve tumor hypoxia and facilitate PDT efficiency.[11] Thus, we further evaluate the tumor hypoxia status after the photothermal treatment using the hypoxia staining probe. As shown in Figs. 6D and S12, the 4T1 tumor-bearing mouse without laser irradiation exhibited large tumor hypoxia areas in the tumor biopsy. By contrast, the tumor hypoxia was significantly relieved after an 808 nm laser irradiation (2 W cm^{-2}, 5min), and the relieved hypoxia condition would benefit the PDT efficacy of Ce6. Moreover, Ce6 in the FRET pair-based nanoassembly could be readily unlocked upon the photobleaching of DiR, with distinctly increased fluorescence intensity of Ce6 after an 808 nm laser irradiation (Fig. 6E). These *in vivo* results indicated that FRET pair-based Ce6@DiR-M NPs, with promoted deep penetration, relieved tumor hypoxia, and on-demand activation of Ce6, could have the cascaded PTT/PDT therapeutic advantages.

2.9. *In vivo* programmed cancer synergistic phototherapy

We then evaluated the *in vivo* synergetic therapeutic effects of Ce6@DiR-M NPs in a 4T1 tumor-bearing mouse xenograft model. Saline, DiR Sol, Ce6 Sol, Ce6@DiR NPs, and Ce6@DiR-M NPs were intravenously administrated to the mice for a total of five injections separately, with an equivalent dosage of 1.9 mg kg^{-1} Ce6 and 5.0 mg kg^{-1} DiR. The Ce6@DiR NPs-, and Ce6@DiR-M NPs- treated groups received 808-nm laser irradiation (2.0 W cm^{-2}, 5 min) at 12 h post-administration for promoting deep penetration and relieving tumor hypoxia. Then, they further received sequential 808-nm laser irradiation (2.0 W cm^{-2}, 5 min) and 660-nm laser irradiation (10 mW cm^{-2}, 5 min) at 24 h post-administration for combination therapy of PTT and PDT (Fig. 7A). The Ce6@DiR-M NPs-treated group received only 660-nm laser irradiation (10 mW cm^{-2}, 5 min) was utilized as Ce6-inactivated control, in which Ce6 was quenched by DiR. The Ce6 Sol treated group and DiR Sol treated group received 660-nm laser irradiation (10 mW cm^{-2}, 5 min) and 808-nm laser irradiation (2.0 W cm^{-2}, 5 min), respectively. As shown in Fig. 7B, since Ce6 was in a quenched state, the Ce6@DiR-M NPs-treated group with single 660-nm laser irradiation showed a rapid increase in tumor volume, having no significant difference with the saline-treated group. Compared with DiR Sol or Ce6 Sol treated group, Ce6@DiR NPs demonstrated a slight therapeutic advantage, but the tumor volume also increased quickly. By contrast, under cascaded local laser irradiation of 808 nm and 660 nm, mice treated with Ce6@DiR-M NPs exhibited potent antitumor activity, with almost no significant progression in tumor growth. Similar results were observed in the tumor burdens of mice at 14 days post-administration (Fig. 7C). These results demonstrated the therapeutic advantages of the biomimetic nanoassembly in synergetic PTT/PDT combination treatment. Moreover, no

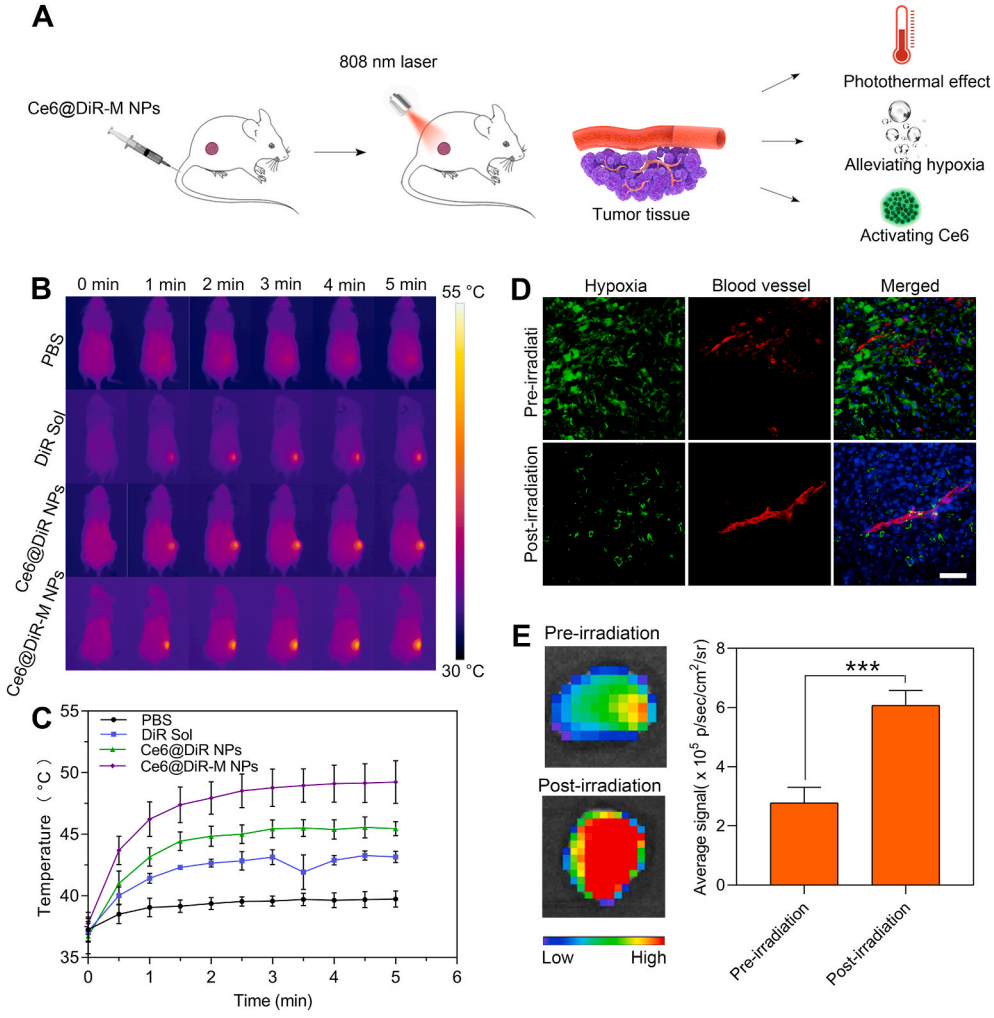

Fig. 6. *In vivo* photothermal effect and modulation of the tumor hypoxia. (A) Schematic illustration of DiR induced photothermal effect, hypoxia alleviation, and Ce6 activation. (B) *In vivo* photothermal images and (C) temperature changing curves under 808-nm laser irradiation (2 W cm^{-2}, 5min). (D) Immunofluorescence staining assay images of tumor sections from mice injected with Ce6@DiR-M NPs after 808-nm laser irradiation (2 W cm^{-2}, 5min) (Scale bar represents 50 μm). (E) Pre- and post-irradiation (808-nm laser, 2 W cm^{-2}, 5min) fluorescence images and quantitative results of Ce6 signals from the tumor after 24 h injection of Ce6@DiR-M NPs. The data are presented as means ± SD, *P < 0.05, **P < 0.01, and ***P < 0.001.

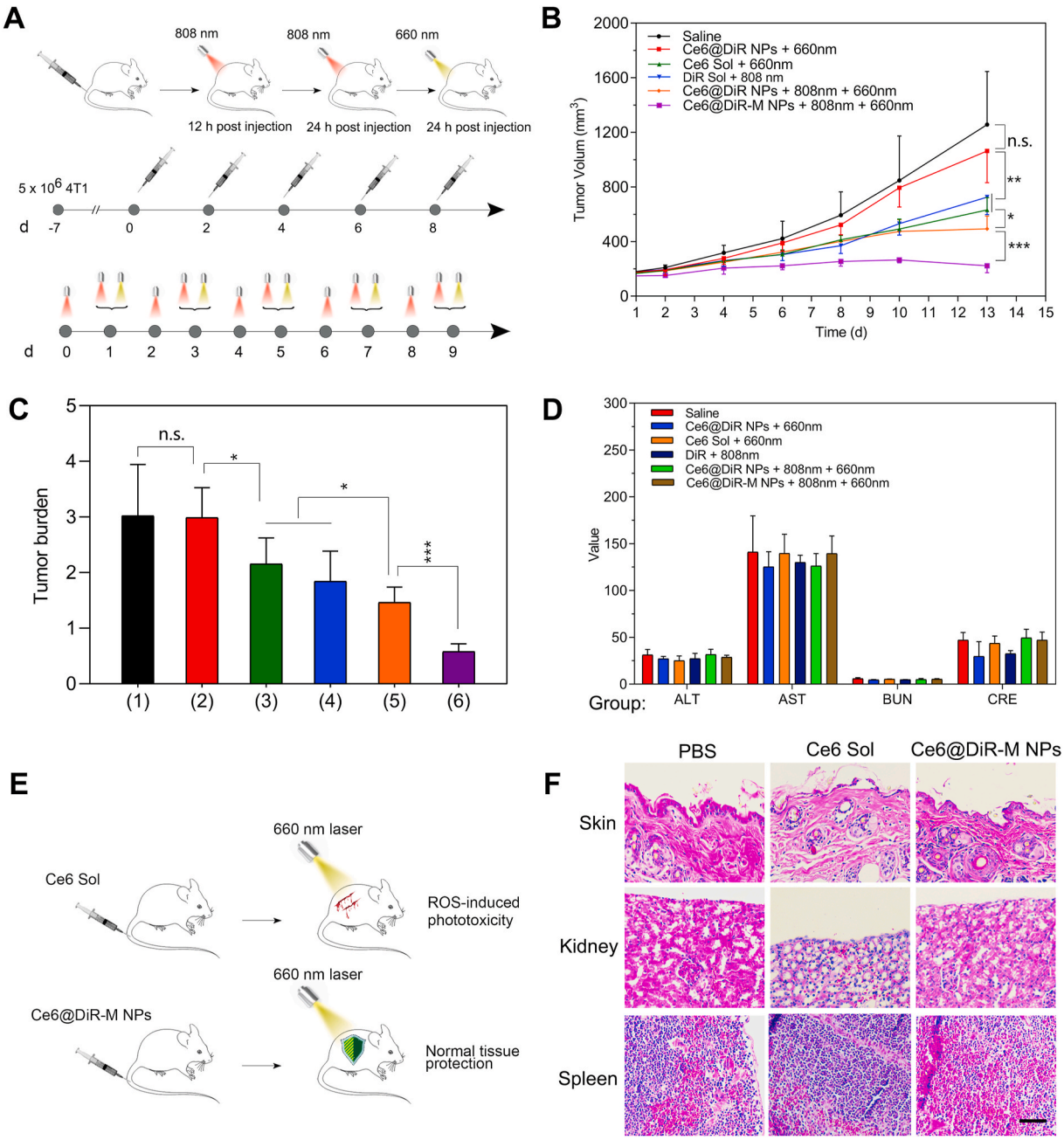

Fig. 7. ***In vivo*** **antitumor efficacy and reducing phototoxicity.** (A) Therapeutic protocol on 4T1 breast cancer bearing mice (660 nm laser: 10.0 mW cm^{-2}, 5 min; 808 nm laser: 2.0 W cm^{-2}, 5 min); (B) Tumor growth profiles with different treatments (There's no mice died during the treatment period.); (C) Tumor burden: (1) Saline, (2) Ce6@DiR-M NPs + 660 nm, (3) Ce6 Sol + 660 nm, (4) DiR Sol + 808 nm, (5) Ce6@DiR NPs + 808 nm + 660 nm and (6) Ce6@DiR-M NPs + 808 nm + 660 nm; (D) Hepatorenal function evaluation (AST: aspartate aminotransferase (U L^{-1}); ALT: alanine aminotransferase (U L^{-1}), BUN: blood urea nitrogen (mmol L^{-1}), CREA: creatinine (μmol L^{-1})); (E) Schematic illustration of phototoxicity-reducing of Ce6@DiR-M NPs; (F) H&E stain of skin, spleen, and kidney after the 660-nm laser (5 mW cm^{-2} for 1h) treatment (Scale bar represents 50 μm). The data are presented as means ± SD, *P < 0.05, **P < 0.01, and ***P < 0.001.

significant changes in hepatorenal function or body weight were found in any group and no obvious histological damage was observed in major organs during the treatment (Figs. 7D, S13, S14).

2.10. *Alleviating ROS-inducing phototoxicity to normal tissues*

Moreover, we supposed that such a uniquely engineered co-delivery nanosystem fabricated by FRET-paired PSs not only had a synergistic therapeutic effect but also effectively address the problem of ROS-induced phototoxicity (Fig. 7E). Therefore, we further explored the phototoxicity of the skin and near-skin organs (spleen and kidney) of Ce6@DiR-M NPs *in vivo*. Three groups of hair-removed healthy Balb/c mice were injected with saline, Ce6 Sol and Ce6@DiR-M NPs, respectively, then exposed to 660-nm laser irradiation (5 mW cm^{-2} for 1 h) at 2 h post-injection. At 12 h post-irradiation, skin, kidney, and spleen were collected for histology analysis. As shown in Fig. 7F, no obvious histological damage was observed in the Ce6@DiR-M NPs-treated group when compared with saline control. On the contrary, skins and kidneys of those mice treated with Ce6 Sol had a distinctly necrotic area than that of the saline control group and Ce6@DiR-M NPs treated group. These results indicated that the Ce6@DiR-M NPs, with excellent antitumor activity, could efficiently deal with the ROS-inducing phototoxicity to the skin and other superficial organs during PDT, which must be beneficial to the clinical translation of PDT-based nanotherapeutics.

3. Conclusions

In summary, we verified the FRET pairs co-assembly strategy with dual-mode photosensitizer co-loading and phototoxicity locking for programmed cancer synergistic phototherapy. The erythrocyte camouflaged co-assembled FRTE-pair (Ce6@DiR-M NPs) displayed prolonged circulation time in the blood, favorable tumor accumulation, and deep tumor penetration *in vivo*. Under cascaded local laser irradiation, the biomimetic nanoassembly demonstrating synergetic photothermal/photodynamic therapy in the TNBC mouse xenograft model. More importantly, such a uniquely co-assembled nanosystem of FRET-paired PSs could effectively address the problem of ROS-induced phototoxicity *in vivo*. The present study solves several key problems related to the dilemmas in cancer phototherapy: (i) unsatisfactory therapeutic efficacy of mono-phototherapy; (ii) photoinduced oxidative damage to normal tissues; (iii) potential toxicity of nanocarrier excipients materials; and (iv) complex preparation process of nanocarriers for combination delivery of photosensitizers. Therefore, such a unique nanoplatform, integrating multiple drug delivery advantages into one system with high-efficient co-loading and co-delivery characteristics, is promising to overcome a series of barriers in combined phototherapy.

4. Experimental section

4.1. Materials

Ce6, DiR, BDP, PPa, Hy, and SOSG were obtained from Meilun Biotech Co. Ltd, China. The anti-CD47 antibody was acquired from Biosynthesis Biotechnology Inc, China. Shanghai Advanced Vehicle Technology Co. Ltd. provided DSPE-PEG_{2k}. Vessels for cell culture were supplied by Wuxi NEST Biotechnology Co., Ltd, China. Fetal bovine serum (FBS) and cell culture media were provided from GIBCO, Invitrogen Corp. The anti-CD31 antibody was purchased from Beijing Solarbio Science & Technology Co., Ltd, China. The solvents and reagents used in this study were all of the analytical grades.

4.2. Preparation of PDP@PTP co-assembly

PDP (BDP, Hy, ZnPc, and PPa) and PTP (DiR) was separately dissolved in dimethyl sulfoxide, then the mixed solution of PDP and PTP with a molar ratio of 1:2 (PDP: PTP) in 100 μL, was added in a stirred deionized water. The product was further ultra-filtered to remove the organic solution and adjust the volume to make the final concentration of 0.1 mg/mL. Characterization of the co-assembly was the same as Ce6@DiR NPs.

4.3. Preparation of Ce6@DiR NPs

Ce6@DiR NPs were prepared through nanoprecipitation [36]. Briefly, DiR was dissolved in ethanol (5 mg/mL) and Ce6 was dissolved in tetrahydrofuran (THF) (5 mg/mL). Then, a mixing solution with a different molar ratio of Ce6 and DiR was diluted with a mixing solution of ethanol and THF (volume ratio = 2:1) to make a 300 μL organic solution. The mixing solution was injected into 2 mL of water away from light under a stirring rate of 2000 rpm. 5 min afterward, the product was further evaporated to remove the organic solution and adjust the volume.

4.4. Preparation of Ce6@DiR-M NPs and Ce6@DiR-PEG NPs

To obtain the fragment of the red blood cell membrane (RBCM), RBCs from SD rats were carefully washed by 1 × PBS three times. After PBS was removed, the RBCs were incubated in 0.25 × PBS (the hypotonic medium) at 4 °C for 3 h. Then, the fully cracked RBCs were centrifuged (10000 × g, 10 min) and repeatedly washed with ice-cold water three times. The collected RBCM was resuspended and sonicated by probe sonicator (Scientz-IID Ultrasonic Homogenizer, Ningbo Scientz Biotechnology Co., Ltd, China) for 5 min, and then freeze-dried and kept at −80 °C for the following experiments.

To coat the Ce6@DiR NPs, RBCM were redissolved and sonicated (100W, 10min) and then mixed with Ce6@DiR NPs at a different mass ratio. The appropriate ratio was selected by Dynamic light scattering. The selected mixture was then extruded through a series of water-phase filters (400 nm, 200 nm, and 100 nm) for at least 10 cycles. The obtained Ce6@DiR-M NPs were kept at 4 °C. The colloid stability of Ce6@DiR-M NPs was further studied in PBS with 10% fetal bovine serum (FBS).

To prepare the PEGylated Ce6@DiR NPs, DSPE-PEG_{2K} (20 wt%) dissolved in ethanol (5mg mL^{-1}) was added to the Ce6@DiR NPs before the organic solution was evaporated.

4.5. Characterization of the co-assemblies

The zeta potential and hydrodynamic size of Ce6@DiR NPs and Ce6@DiR-M NPs were determined by the Zetasizer. The morphologies of NPs were observed using a transmission electron microscope (TEM) (Hitachi, HT7700, Japan). The samples were stained by phosphotungstic acid (1%, w/v) before visualization.

For the characterization of CD47 on RBCM, sodium dodecyl sulfate-polyacrylamide gel electrophoresis (SDS-PAGE) and western blotting were employed according to the previously published protocol [17]. Briefly, a protein extraction kit (Dingguo, China) was used to extract the total cellular protein of the samples, then the extracted proteins were separated and stained by Coomassie blue. For western blotting, another isolated proteins were transferred to polyvinylidene fluoride (PVDF) membranes (Bio-Rad). The PVDF membranes were then blocked using 5% skim milk. After antibody incubation, the PVDF membranes were treated with ECL Western Blotting Substrate (Meilun Biotech Co. Ltd, China) for developing the blots.

4.6. Self-assembly simulation

The molecular interaction and the mechanism of co-assembly were explored using molecular docking. The molecular structures of DiR and Ce6 were constructed in JSME and MMFF94 force field with energy minimization. The semi-flexible docking was performed in AutoDock Vina. After internal clustering, nine poses were output.

4.7. In vitro photothermal effect

The photothermal effect of Ce6@ DiR-M NPs was measured by a thermal imaging system (Fotric 226). Different concentrations of Ce6@DiR-M NPs were exposed to an 808 nm laser (L808) (MDL-N-5W, Changchun New Industries, China) (2.0 W cm^{-2}, 3 min), and the temperature rising in the process was recorded. The size distribution of the laser-treated agents was acquired using the methods mentioned above.

4.8. Spectrum scanning

Ce6 Sol, DiR Sol, Ce6@DiR NPs, and Ce6@DiR-M NPs at an equivalent Ce6 concentration of 25 μg mL^{-1} or DiR concentration of 64 μg mL^{-1} was added into the 96-well plates, and then fluorescence spectra or UV spectra were then obtained by the Varioskan Flash multimode microreader. After irradiated by L808 (1.0 W cm^{-2}, 5 min), the spectra of the irradiated agents were acquired.

4.9. In vitro singlet oxygen generation capacity

The singlet oxygen sensor green reagent (SOSG) kit was used to evaluate the production of singlet oxygen [14]. Ce6@DiR NPs and Ce6@DiR-M NPs before and after L808 irradiation, as well as Ce6 Sol, were mixed with SOSG at an equivalent Ce6 concentration of 3 μM and SOSG concentration of 2 μM. The samples were then irradiated by a 660

nm laser (L660) (10 mW cm^{-2}, 5 min) and kept at 37 °C. At predetermined time, singlet oxygen was measured by the Varioskan Flash multimode microreader (excitation at 504 nm, emission at 525 nm).

4.10. Cellular uptake

4T1 cells were cultured in cell culture medium (RPMI-1640, containing penicillin-streptomycin and 10% FBS). To investigate the cellular uptake, the 4T1 cells (1×10^5 cells) were incubated with Ce6 Sol, Ce6@DiR NPs, and Ce6@DiR-M NPs (400 ng mL^{-1} of Ce6) for 0.5 and 2 h. Another two groups of cells incubated with Ce6@DiR NPs and Ce6@DiR-M NPs were irradiated with L808 (1W cm^{-2}, 5 min) after incubation. Then all the cells were washed and fixed. After staining by Hoechst, cell imagines were obtained through confocal laser scanning microscopy. FACSCalibur flow cytometer was used for quantitative analysis.

4.11. Intracellular oxidative stress

After incubated with Ce6@DiR NPs/Ce6@DiR-M NPs for 2 h, the cells were processed with different laser treatment, which was consistent with the above description. Then, the intracellular oxidative stress was measured using DCFH-DA according to the instruction.

4.12. Tumor spheroids penetration

Tumor spheroids were constructed in ultra-low-cell-adhesion 24-well plates and cultured for 4 days. Then the tumor spheroids were incubated with Ce6 Sol and Ce6@DiR-M NPs for 4 h. Another Ce6@DiR-M NPs treated cell spheroids was irradiated with L808 (3 W cm^{-2}, 3 min) at 2 h after incubation and kept cultured for another 2 h. Before the observation, all of the cells were irradiated by L808 (1 W cm^{-2}, 5 min).

4.13. Cytotoxicity

The cytotoxicity of locked PDT, single PDT, or combined PTT and PDT were evaluated on 4T1 cells (2.0×10^3). To evaluate the *in vitro* combined PTT and PDT, 4T1 cells were cultured with different concentrations of DiR Sol, Ce6 Sol, Ce6@DiR NPs, and Ce6@DiR-M NPs. After 12 h incubation, the cells were exposed to L808 (3.0 W cm^{-2}, 3 min) or L660 (1.5 mW cm^{-2}, 5 min), or a sequential 808-660 nm laser according to the different groups. To evaluate the cytotoxicity of Ce6 in a quenched and activated state, 4T1 cells were incubated with Ce6 Sol, Ce6@DiR NPs, and Ce6@DiR-M NPs. After 2 h, Ce6@DiR NPs and Ce6@DiR-M NPs -incubated cells were irradiated with a mild L808 (1 W cm^{-2}, 5 min) to exhaust DiR. Finally, 4T1 cells were irradiated with L660 (1.5 mW cm^{-2}, 5 min) before MTT assay. For the dark toxicity evaluation, cells incubated with the above formulation were cultured out of light before the MTT assay. To evaluate the phototoxicity of Ce6@DiR-M NPs with mild L808 (1 W cm^{-2}, 5 min), cells incubated with different concentrations of the formulation were irradiated at 12 h and performed MTT assay at 36 h.

4.14. Haemolysis assay

Ce6@DiR NPs/Ce6@DiR-M NPs (50 μg mL^{-1}) were incubated with RBC (50 μL) at 37 °C in PBS. The haemoglobin released was determined by spectrophotometrically detecting the supernatant of the mixture after centrifugation (A541 nm). RBC lysis buffer treated RBC were used as 100% lysis control.

4.15. Animal studies

Experiments with animals were permitted by the Institutional Animal Ethical Care Committee of Shenyang Pharmaceutical University.

4.16. Pharmacokinetics

Male Sprague-Dawley (SD) rats weighing 190–230 g were utilized. DiR Sol, Ce6@DiR NPs, Ce6@DiR-PEG NPs, and Ce6@DiR-M NPs were intravenously injected (equivalent DiR dosage of 1 mg kg^{-1}, n = 5). At the pre-set time points, blood samples were collected. DiR were extracted by four volumes of methanol, then the concentration of DiR was measured by spectrofluorimetry (ex/em of 748/780 nm). To investigate the pharmacokinetics of the second dose, SD rats were firstly injected with Ce6@DiR-M NPs or Ce6@DiR-PEG NPs. The plasma was obtained and kept at −80 °C before determination. 5 days later, the rats were injected with a second dose which was the same as the first time. Then plasma was collected and measured with the first batch.

4.17. Biodistributions

4T1 xenograft tumors bearing BALB/c mice were established by subcutaneously inoculating 4T1 cells (5×10^6 cells) to female Balb/c mice. DiR Sol, Ce6@DiR NPs, and Ce6@DiR-M NPs (2 mg kg^{-1} of DiR) were intravenously injected. At predetermined time intervals, the mice were anesthetized. Animal fluorescences of DiR were recorded by the small animal imaging system. At 24 h, the mice were sacrificed. Tumors and the main organs were further quantitatively analyzed. To evaluate the activation of Ce6 *in vivo* by L808, mice were injected with Ce6@DiR-M NPs. 24 h later, a group of them were irradiated with L808 (2 W cm^{-2}, 5 min). Then, all of these mice were sacrificed and tumors were brought out for imaging analysis.

4.18. In vivo photothermal efficacy

DiR Sol, Ce6@DiR NPs, and Ce6@DiR-M NPs (2 mg kg^{-1} of DiR) were intravenously injected into the 4T1 xenograft tumors bearing BALB/c mice. 24 h post-injection, the mice were irradiated with an L808 (2 W cm^{-2}, 5 min). At pre-set time intervals, temperature changes were recorded.

4.19. Evaluation of tumor hypoxia

The hypoxia state of tumor tissues was evaluated using the pimonidazole hydrochloride (Hypoxyprobe™, USA) according to the instruction. Briefly, the 4T1 tumor-bearing mice were intravenously administrated of Ce6@DiR-M NPs (5 mg kg^{-1} of DiR). 24 h later, the mice were irradiated with L808 (2.0 W cm^{-2}, 5 min). Then 1.5 mg of pimonidazole hydrochloride was intraperitoneally injected to each mice. After 90 min, tumor tissues were collected as formalin-fixed and paraffin-embedded tissue samples for immunostaining. CD31 antibody and Hyproxyprobe-1 MAb1 were used for the stain of blood vessels and the hypoxia region. After a secondary antibody incubation, the sample was observed by the fluorescence microscope.

4.20. In vivo antitumor efficacy

The antitumor phototherapy study was carried out in the 4T1 xenograft tumors bearing BALB/c mice. When the tumors volume was around 200 mm^3, the mice were randomly divided in: i) saline control; ii) Ce6 Sol with L660 (10.0 mW cm^{-2}, 5 min); iii) DiR Sol with L808 (2.0 W cm^{-2}, 5 min); iv) Ce6@DiR-M NPs with single L660; v) and vi) Ce6@DiR NPs and Ce6@DiR-M NPs with sequential 808 and 660 nm laser irradiation (L808: 2.0 W cm^{-2} and 5 min; L660: 10.0 mW cm^{-2} and 5 min). The formulations (at an equivalent dosage of 1.9 mg kg^{-1} of Ce6 or 2.0 mg kg^{-1} of DiR) were intravenously administrated to the mice every other day for a total of five injections. At 12 h post-administration, the mice were irradiated with L808 (2.0 W cm^{-2}, 5 min). And at 24 after administration, the mice were treated according to the description. The tumor volume and body weight changes were recorded every two days. All the operations were performed out of light. The blood was collected

for hepatic and renal function analysis after the mice were sacrificed. Tumor tissues and major organs were collected. H&E staining was performed for the evaluation of pathological changes.

4.21. In vivo photo-toxicity of Ce6@DiR-M NPs

The *in vivo* photo-toxicity was studied using hair-removed mice. These mice were intravenously injected with Ce6 Sol and Ce6@DiR-M NPs (n = 3) at equivalent Ce6 doses of 3.0 mg kg^{-1}. At 3 h after administration, all of the mice were exposed to L660 (5.0 mW cm^{-2}, 1 h). At 8 h post-treatment, the mice were sacrificed, skin, kidney, and spleen were harvest for H&E staining.

4.22. Statistical analysis

Data were presented as mean ± SD. Statistical analysis was performed using an unpaired two-tailed *t*-test. P value less than 0.05 was considered statistically significant differences.

CRediT authorship contribution statement

Xuanbo Zhang: Conceptualization, Investigation, Validation, Supervision, Writing - original draft, Visualization. **Jianchen Xiong:** Resources, Validation, Investigation. **Kaiyuan Wang:** Resources, Investigation, Methodology. **Han Yu:** Investigation. **Bingjun Sun:** Investigation, Project administration. **Hao Ye:** Methodology. **Zhiqiang Zhao:** Investigation. **Ning Wang:** Investigation. **Yuequan Wang:** Investigation. **Shenwu Zhang:** Investigation. **Wutong Zhao:** Investigation. **Haotian Zhang:** Resources. **Zhonggui He:** Funding acquisition, Project administration. **Cong Luo:** Funding acquisition, Project administration, Conceptualization, Supervision, Writing - review & editing. **Jin Sun:** Funding acquisition, Project administration, Supervision, Writing - review & editing.

Declaration of competing interest

The authors declare that they have no known competing financial interests or personal relationships that could have appeared to influence the work reported in this paper.

Acknowledgments

This work was supported by the National Natural Science Foundation of China (No. 81773656 and 81703451), the Excellent Youth Science Foundation of Liaoning Province (No. 2020-YQ-06), the China Postdoctoral Science Foundation (No. 2020M670794) and the Liaoning Revitalization Talents Program (No. XLYC1907129 and XLYC1808017), the Science and Technology Major Project of Liaoning (No. 2019JH1/10300004) and the National College Students' innovation and entrepreneurship training program (No. 201910163200).

Appendix A. Supplementary data

Supplementary data to this article can be found online at https://doi.org/10.1016/j.bioactmat.2021.01.004.

References

[1] A.G. Waks, E.P. Winer, Breast cancer treatment a review, JAMA, J. Am. Med. Assoc. 321 (3) (2019) 288–300, https://doi.org/10.1001/jama.2018.19323.
[2] R.L. Siegel, K.D. Miller, A. Jemal, Cancer statistics, 2020. CA, Canc. J. Clin. 70 (1) (2020) 7–30, https://doi.org/10.3322/caac.21590.
[3] J.R. Baker, J.A. Sakoff, A. McCluskey, The aryl hydrocarbon receptor (ahr) as a breast cancer drug target, Med. Res. Rev. 40 (3) (2020) 972–1001, https://doi.org/10.1002/med.21645.
[4] X. Shan, S. Li, B. Sun, Q. Chen, J. Sun, Z. He, C. Luo, Ferroptosis-driven nanotherapeutics for cancer treatment, J. Contr. Release : Off. J. Controll. Release Soc. 319 (2020) 322–332, https://doi.org/10.1016/j.jconrel.2020.01.008.
[5] C. Kim, R.L. Gao, E. Sei, R. Brandt, J. Hartman, T. Hatschek, N. Crosetto, T. Foukakis, N.E. Navin, Chemoresistance evolution in triple-negative breast cancer delineated by single-cell sequencing, Cell 173 (4) (2018) 879, https://doi.org/10.1016/j.cell.2018.03.041.
[6] K. Wang, H. Ye, X. Zhang, X. Wang, B. Yang, C. Luo, Z. Zhao, J. Zhao, Q. Lu, H. Zhang, Q. Kan, Y. Wang, Z. He, J. Sun, An exosome-like programmable-bioactivating paclitaxel prodrug nanoplatform for enhanced breast cancer metastasis inhibition, Biomaterials 257 (2020), https://doi.org/10.1016/j.biomaterials.2020.120224.
[7] K.Y. Wang, B. Yang, H. Ye, X.B. Zhang, H. Song, X. Wang, N. Li, L. Wei, Y. Wang, H. T. Zhang, Q.M. Kan, Z.G. He, D. Wang, J. Sun, Self-strengthened oxidation-responsive bioactivating prodrug nanosystem with sequential and synergistically facilitated drug release for treatment of breast cancer, ACS Appl. Mater. Interfaces 11 (21) (2019) 18914–18922, https://doi.org/10.1021/acsami.9b03056.
[8] F. Yang, Z. Zhao, B. Sun, Q. Chen, J. Sun, Z. He, C. Luo, Nanotherapeutics for antimetastatic treatment, Trends Canc. 6 (8) (2020) 645–659, https://doi.org/10.1016/j.trecan.2020.05.001.
[9] S. Li, X. Shan, Y. Wang, Q. Chen, J. Sun, Z. He, B. Sun, C. Luo, Dimeric prodrug-based nanomedicines for cancer therapy, J. Contr. Release : Off. J. Controll. Release Soc. 326 (2020) 510–522, https://doi.org/10.1016/j.jconrel.2020.07.036.
[10] X.H. Pu, J. Li, P. Qiao, M.M. Li, H.Y. Wang, L.L. Zong, Q. Yuan, S.F. Duan, Mesoporous silica nanoparticles as a prospective and promising approach for drug delivery and biomedical applications, Curr. Cancer Drug Targets 19 (4) (2019) 285–295, https://doi.org/10.2174/1568009619666181206114904.
[11] R. van der Meel, E. Sulheim, Y. Shi, F. Kiessling, W.J.M. Mulder, T. Lammers, Smart cancer nanomedicine, Nat. Nanotechnol. 14 (11) (2019) 1007–1017, https://doi.org/10.1038/s41565-019-0567-y.
[12] B.J. Sun, C. Luo, H. Yu, X.B. Zhang, Q. Chen, W.Q. Yang, M.L. Wang, Q.M. Kan, H. T. Zhang, Y.J. Wang, Z.G. He, J. Sun, Disulfide bond-driven oxidation- and reduction-responsive prodrug nanoassemblies for cancer therapy, Nano Lett. 18 (6) (2018) 3643–3650, https://doi.org/10.1021/acs.nanolett.8b00737.
[13] B.J. Sun, C. Luo, X.B. Zhang, M.R. Guo, M.C. Sun, H. Yu, Q. Chen, W.Q. Yang, M. L. Wang, S.Y. Zuo, P.Y. Chen, Q.M. Kan, H.T. Zhang, Y.J. Wang, Z.G. He, J. Sun, Probing the impact of sulfur/selenium/carbon linkages on prodrug nanoassemblies for cancer therapy, Nat. Commun. 10 (1) (2019), https://doi.org/10.1038/s41467-019-11193-x.
[14] C. Luo, B.J. Sun, C. Wang, X.B. Zhang, Y. Chen, Q. Chen, H. Yu, H.Q. Zhao, M. C. Sun, Z.B. Li, H.T. Zhang, Q.M. Kan, Y.J. Wang, Z.G. He, J. Sun, Self-facilitated ros-responsive nanoassembly of heterotypic dimer for synergistic chemo-photodynamic therapy, J. Contr. Release 302 (2019) 79–89, https://doi.org/10.1016/j.jconrel.2019.04.001.
[15] K. Cheng, X.Q. Yang, X.S. Zhang, J. Chen, J. An, Y.Y. Song, C. Li, Y. Xuan, R. Y. Zhang, C.H. Yang, X.L. Song, Y.D. Zhao, B. Liu, High-security nanocluster for switching photodynamic combining photothermal and acid-induced drug compliance therapy guided by multimodal active-targeting imaging, Adv. Funct. Mater. 28 (36) (2018), https://doi.org/10.1002/adfm.201803118.
[16] L.Z. Feng, D.L. Tao, Z.L. Dong, Q. Chen, Y. Chao, Z. Liu, M.W. Chen, Near-infrared light activation of quenched liposomal ce6 for synergistic cancer phototherapy with effective skin protection, Biomaterials 127 (2017) 13–24, https://doi.org/10.1016/j.biomaterials.2016.11.027.
[17] H. Ye, K. Wang, M. Wang, R. Liu, H. Song, N. Li, Q. Lu, W. Zhang, Y. Du, W. Yang, L. Zhong, Y. Wang, B. Yu, H. Wang, Q. Kan, H. Zhang, Y. Wang, Z. He, J. Sun, Bioinspired nanoplatelets for chemo-photothermal therapy of breast cancer metastasis inhibition, Biomaterials 206 (2019) 1–12, https://doi.org/10.1016/j.biomaterials.2019.03.024.
[18] N. Zhang, M.H. Li, X.T. Sun, H.Z. Jia, W.G. Liu, Nir-responsive cancer cytomembrane-cloaked carrier-free nanosystems for highly efficient and self-targeted tumor drug delivery, Biomaterials 159 (2018) 25–36, https://doi.org/10.1016/j.biomaterials.2018.01.007.
[19] Y. Li, G.H. Liu, J.Y. Ma, J.Y. Lin, H.R. Lin, G.H. Su, D.Y. Chen, S.F. Ye, X.Y. Chen, X. Zhu, Z.Q. Hou, Chemotherapeutic drug-photothermal agent co-self-assembling nanoparticles for near-infrared fluorescence and photoacoustic dual-modal imaging-guided chemo-photothermal synergistic therapy, J. Contr. Release 258 (2017) 95–107, https://doi.org/10.1016/j.jconrel.2017.05.011.
[20] Z. Fan, H. Liu, Y. Xue, J. Lin, Y. Fu, Z. Xia, D. Pan, J. Zhang, K. Qiao, Z. Zhang, Y. Liao, Reversing cold tumors to hot: an immunoadjuvant-functionalized metal-organic framework for multimodal imaging-guided synergistic photo-immunotherapy, Bioact. Mater. 6 (2) (2021) 312–325, https://doi.org/10.1016/j.bioactmat.2020.08.005.
[21] M. Wen, J. Ouyang, C. Wei, H. Li, W. Chen, Y.N. Liu, Artificial enzyme catalyzed cascade reactions: antitumor immunotherapy reinforced by nir-ii light, Angew Chem. Int. Ed. Engl. 58 (48) (2019) 17425–17432, https://doi.org/10.1002/anie.201909729.
[22] Y. Yang, W.J. Zhu, Z.L. Dong, Y. Chao, L. Xu, M.W. Chen, Z. Liu, 1d coordination polymer nanofibers for low-temperature photothermal therapy, Adv. Mater. 29 (40) (2017), https://doi.org/10.1002/adma.201770293.
[23] W. Chen, K. Zeng, H. Liu, J. Ouyang, L. Wang, Y. Liu, H. Wang, L. Deng, Y.-N. Liu, Cell membrane camouflaged hollow prussian blue nanoparticles for synergistic photothermal-/chemotherapy of cancer, Adv. Funct. Mater. 27 (11) (2017), https://doi.org/10.1002/adfm.201605795.
[24] W. Chen, J. Ouyang, H. Liu, M. Chen, K. Zeng, J. Sheng, Z. Liu, Y. Han, L. Wang, J. Li, L. Deng, Y.N. Liu, S. Guo, Black phosphorus nanosheet-based drug delivery system for synergistic photodynamic/photothermal/chemotherapy of cancer, Adv. Mater. 29 (5) (2017), https://doi.org/10.1002/adma.201603864.

[25] Q. Chen, G.X. Liu, S. Liu, H.Y. Su, Y. Wang, J.Y. Li, C. Luo, Remodeling the tumor microenvironment with emerging nanotherapeutics, Trends Pharmacol. Sci. 39 (1) (2018) 59–74, https://doi.org/10.1016/j.tips.2017.10.009.
[26] J. Sheng, L. Zhang, L. Deng, Y. Han, L. Wang, H. He, Y.-N. Liu, Fabrication of dopamine enveloped wo3−x quantum dots as single-nir laser activated photonic nanodrug for synergistic photothermal/photodynamic therapy against cancer, Chem. Eng. J. 383 (2020), https://doi.org/10.1016/j.cej.2019.123071.
[27] C.H. Liu, D.D. Wang, S.Y. Zhang, Y.R. Cheng, F. Yang, Y. Xing, T.L. Xu, H.F. Dong, X.J. Zhang, Biodegradable biomimic copper/manganese silicate nanospheres for chemodynamic/photodynamic synergistic therapy with simultaneous glutathione depletion and hypoxia relief, ACS Nano 13 (4) (2019) 4267–4277, https://doi.org/10.1021/acsnano.8b09387.
[28] K. Zhang, X.D. Meng, Y. Cao, Z. Yang, H.F. Dong, Y.D. Zhang, H.T. Lu, Z.J. Shi, X. J. Zhang, Metal-organic framework nanoshuttle for synergistic photodynamic and low-temperature photothermal therapy, Adv. Funct. Mater. 28 (42) (2018), https://doi.org/10.1002/adfm.201804634.
[29] W.W.L. Chin, W.K.O. Lau, P.W.S. Heng, R. Bhuvaneswari, M. Olivo, Fluorescence imaging and phototoxicity effects of new formulation of chlorin e6-polyvinylpyrrolidone, J. Photochem. Photobiol., B 84 (2) (2006) 103–110, https://doi.org/10.1016/j.jphotobiol.2006.02.002.
[30] X. Li, J.F. Lovell, J. Yoon, X. Chen, Clinical development and potential of photothermal and photodynamic therapies for cancer, Nat. Rev. Clin. Oncol. (2020), https://doi.org/10.1038/s41571-020-0410-2.
[31] B.J. Sun, Y. Chen, H. Yu, C. Wang, X.B. Zhang, H.Q. Zhao, Q. Chen, Z.G. He, C. Luo, J. Sun, Photodynamic peg-coated ros-sensitive prodrug nanoassemblies for core-shell synergistic chemo-photodynamic therapy, Acta Biomater. 92 (2019) 219–228, https://doi.org/10.1016/j.actbio.2019.05.008.
[32] X.B. Zhang, B.J. Sun, S.Y. Zuo, Q. Chen, Y.L. Gao, H.Q. Zhao, M.C. Sun, P.Y. Chen, H. Yu, W.J. Zhang, K.Y. Wang, R.S. Zhang, A.M. Kan, H.T. Zhang, Z.G. He, C. Luo, J. Sun, Self-assembly of a pure photosensitizer as a versatile theragnostic nanoplatform for imaging-guided antitumor photothermal therapy, ACS Appl. Mater. Interfaces 10 (36) (2018) 30155–30162, https://doi.org/10.1021/acsami.8b10421.
[33] X. Zhang, N. Li, S. Zhang, B. Sun, Q. Chen, Z. He, C. Luo, J. Sun, Emerging carrier-free nanosystems based on molecular self-assembly of pure drugs for cancer therapy, Med. Res. Rev. 40 (5) (2020) 1754–1775, https://doi.org/10.1002/med.21669.
[34] C. Luo, B. Sun, C. Wang, X. Zhang, Y. Chen, Q. Chen, H. Yu, H. Zhao, M. Sun, Z. Li, H. Zhang, Q. Kan, Y. Wang, Z. He, J. Sun, Self-facilitated ros-responsive nanoassembly of heterotypic dimer for synergistic chemo-photodynamic therapy, J. Contr. Release : Off. J. Controll. Release Soc. 302 (2019) 79–89, https://doi.org/10.1016/j.jconrel.2019.04.001.
[35] L. Rao, L.L. Bu, J.H. Xu, B. Cai, G.T. Yu, X.L. Yu, Z.B. He, Q.Q. Huang, A. Li, S. S. Guo, W.F. Zhang, W. Liu, Z.J. Sun, H. Wang, T.H. Wang, X.Z. Zhao, Red blood cell membrane as a biomimetic nanocoating for prolonged circulation time and reduced accelerated blood clearance, Small 11 (46) (2015) 6225–6236, https://doi.org/10.1002/smll.201502388.
[36] C. Luo, J. Sun, B. Sun, D. Liu, L. Miao, T.J. Goodwin, L. Huang, Z. He, Facile fabrication of tumor redox-sensitive nanoassemblies of small-molecule oleate prodrug as potent chemotherapeutic nanomedicine, Small 12 (46) (2016) 6353–6362, https://doi.org/10.1002/smll.201601597.